Electrochimica Acta 543 (2025) 147529

Contents lists available at ScienceDirect

Electrochimica Acta

journal homepage: www.journals.elsevier.com/electrochimica-acta

A comparison of PEM fuel cell parameters resulting from the distribution of relaxation times, distribution of transport times, and physics-based modeling

Tatyana Reshetenko [a], Andrei Kulikovsky [b,*]

[a] Hawaii Natural Energy Institute, University of Hawaii, Honolulu, HI 96822, USA
[b] Forschungszentrum Jülich GmbH, Theory and Computation of Energy Materials (IET–3), Institute of Energy and Climate Research, D–52425 Jülich, Germany

ARTICLE INFO

Dataset link: https://github.com/akulikovsky/DTT_software

Keywords:
Electrochemical impedance spectroscopy
Distribution of relaxation times DRT
Distribution of transport times DTT
Inductive loop
Physics-based impedance modeling
PEM fuel cells

ABSTRACT

Recently, the Distribution of Transport Times (DTT) technique has been suggested as a supplement to the distribution of relaxation times (DRT) technique for analyzing impedance spectra of PEM fuel cells. In this study, we compare the faradaic and transport resistivities obtained from DRT and DTT with those resulting from fitting the physics-based model (PBM) to the experimental spectra. The DTT of the PEMFC impedance without the low-frequency inductive loop yields peak resistivities that closely match those obtained from the PBM, whereas the peak resistivities derived from the DRT are generally less accurate. Moreover, unlike the DRT spectrum, the DTT successfully resolves the transport peak. We propose a modification to the composite kernel used in the DTT to describe spectra with a low-frequency "inductive" loop. An example of DTT calculated from an experimental spectrum containing such a loop is demonstrated.

1. Introduction

Polymer electrolyte membrane (PEM) fuel cells are slowly conquering the market of power sources for heavy-duty mobile applications, such as trains, ships and trucks [1]. Further expansion of PEMFC applications requires development of rapid in situ methods to assess the health of cells and stacks. Non-destructive, non-invasive, operando Electrochemical Impedance Spectroscopy (EIS) is the best technique to solve this task [2].

In the past two decades, a new method for analyzing impedance spectra has emerged: the distribution of relaxation times (DRT) [3–8]. The DRT is a model-free purely math procedure of expansion of cell impedance into an infinite sum of parallel *RC*-circuit impedances. DRT does not require any prior information about the cell; calculating a DRT spectrum from an experimental impedance takes less than a second on a notebook. The result is a number of peaks, each representing one or more transport and/or kinetic processes in the cell.

The classic DRT spectrum $\gamma(\tau)$ obeys the equation

$$Z_{cell}(\omega) = R_\infty + R_{pol}\int_{-\infty}^{\infty} K_D(\omega,\tau)\,\gamma(\tau)\,d\ln\tau \tag{1}$$

where Z_{cell} is the measured cell impedance, R_∞ is the high-frequency (ohmic) resistivity, R_{pol} is the total polarization resistivity of the cell, and K_D is the Debye kernel

$$K_D(\omega,\tau) = \frac{1}{1+i\omega\tau}. \tag{2}$$

Unfortunately, the kernel K_D is not suitable for describing oxygen and proton transport in porous layers. Using this kernel results in the formation of several high-frequency phantom peaks in the DRT spectrum of a PEMFC [7,9,10]. Furthermore, the DRT calculated from Eq. (1) may miss the peaks describing oxygen transport in porous layers [11].

To avoid false peaks and to capture the oxygen transport processes, a composite kernel K_c for replacing K_D in Eq. (1) has been suggested [11]. In the low-frequency domain, K_c reduces to the kernel for oxygen transport in the gas diffusion layer. In the high-frequency domain it reduces to the kernel for proton transport in the cathode catalyst layer (CCL). In the middle-frequency range K_c transforms to the Debye kernel for describing the faradaic impedance. A distribution of transport times (DTT) technique based on the composite kernel has been compared to the DRT using synthetic spectra produced with the physics-based impedance model [11]. The advantage of DTT over the DRT in resolving oxygen and proton transport peaks has been demonstrated.

In the absence of an inductive loop, R_{pol} is the full diameter of the Nyquist spectrum along the real axis. However, PEMFC impedance often contains a low-frequency (LF) "inductive" loop. The nature of this loop is not well understood. Several processes have been suggested in the literature to explain the loop [12–22] (see [23–25] for detailed reviews). In addition, so far there is no fully satisfactory solution to the problem of fitting an inductive loop using the DRT-like technique.

* Corresponding author.
E-mail addresses: tatyanar@hawaii.edu (T. Reshetenko), A.Kulikovsky@fz-juelich.de (A. Kulikovsky).

https://doi.org/10.1016/j.electacta.2025.147529
Received 11 August 2025; Received in revised form 25 September 2025; Accepted 2 October 2025
Available online 14 October 2025

Nomenclature

b	ORR Tafel slope, V
c	Oxygen molar concentration in the CCL, mol cm^{-3}
c_b	Oxygen molar concentration in the GDL, mol cm^{-3}
c_h	Oxygen molar concentration in the channel, mol cm^{-3}
c_v	Water vapor molar concentration mol cm^{-3}
c_v^s	Saturated water concentration at 80 °C
C_{dl}	Double layer capacitance, F cm^{-3}
D_b	Oxygen diffusivity of the GDL, cm^2 s^{-1}
D_{ox}	Oxygen diffusivity of the CCL, cm^2 s^{-1}
$D_{ox,d}$	Oxygen diffusivity of the dry CCL, cm^2 s^{-1}
D_v	Water vapor diffusivity in the CCL, cm^2 s^{-1}
e_0	Elementary charge, C
F	Faraday constant, C mol^{-1}
h	Cathode channel height, cm
i	Imaginary unit
i_*	Volumetric ORR exchange current density, A cm^{-3}
j_0	Cell mean current density, A cm^{-2}
K_l	CCL liquid water permeability, cm^2
k_{pc}	Slope of the water retention curve, Eq. (13), Pa
k_σ	Coefficient in Eq. (14) S cm^{-1}
l_t	CCL thickness, cm
l_b	GDL thickness, cm
p_c	Capillary pressure, Pa
p_l	Liquid phase pressure, Pa
p_g	Gas phase pressure, Pa
p_{cell}	Cathode pressure, Pa
Q_{ORR}	ORR rate, A cm^{-3}
Q_{lv}	Rate of evaporation/condensation, A cm^{-3}
R	Gas constant, J K^{-1} mol^{-1}
R_∞	High frequency cell resistivity, Ohm cm^2
R_i	DTT resistivity of the ith process, Ohm cm^2
R_{pol}	Cell polarization resistivity, Ohm cm^2
R_i^*	True resistivity of the ith process, Ohm cm^2, Eq. (39)
R_{chan}	Resistivity due to oxygen transport in the channel, Ohm cm^2
R_{CCL}	Resistivity due to oxygen transport in the CCL, Ohm cm^2
R_{GDL}	Resistivity due to oxygen transport in the GDL, Ohm cm^2
R_{ORR}	Faradaic resistivity, Ohm cm^2
R_p	Resistivity of proton transport in the CCL, Ohm cm^2
v	Air flow velocity in the channel, cm s^{-1}
x	Coordinate through the cell, cm
z	Coordinate along the channel, cm
Z_{cell}	Cell impedance, Ohm cm^2

Subscripts:

0	membrane/CCL interface
1	CCL/GDL interface
b	GDL
h	Channel

Superscripts:

0	Steady-state value
1	Small-amplitude perturbation

Greek:

α	Step function, Eq. (21)
α_w	Net water transfer coefficient through the membrane
β	Step function, Eq. (21)
γ	DTT function, Eq. (19)
γ_L	DTT function, Eq. (27)
ϵ	Positive constant, Eq. (32)
ζ	Step function, Eq. (25)
η	ORR overpotential, positive by convention, V
λ	Air flow stoichiometry
μ_l	Liquid water kinematic viscosity, Pa s
κ	Vaporization rate constant, atm^{-1} cm^{-2} s^{-1}
ξ_{lv}	The evaporation interfacial area factor
σ_p	CCL proton conductivity, S cm^{-1}
σ_p^*	Reference CCL proton conductivity, S cm^{-1}
τ	Characteristic time constant, s
ω	Angular frequency of the AC signal, s^{-1}

To describe an LF loop, Danzer [26] suggested calculating the DRT function using the series connection of the RC- and RL-elements

$$Z_{cell}(\omega) = R_\infty + R_{pol}\int_{-\infty}^{\infty}\Big(K_D\,\gamma_D(\tau) + K_{RL}\,\gamma_{RL}(\tau)\Big)\,d\ln\tau \tag{3}$$

where

$$K_{RL}(\omega,\tau) = \frac{1}{1+(\mathrm{i}\omega\tau)^{-1}} \tag{4}$$

is the RL-kernel describing the impedance of a parallel RL-circuit. This approach introduces a second DRT function γ_{RL}. Recently Plank et al. [27] suggested using the sum of the Debye and RL-kernels in Eq. (1) keeping a single DRT function $\gamma(\tau)$. In either case, the incorporation of the RL-kernel provides an accurate description of the inductive loop. However, the RL-kernel, Eq. (4), does not vanish as $\omega \to \infty$, which changes the high-frequency (ohmic) cell resistivity. Perturbations of γ in the high-frequency region are multiplied by the kernel $K_{RL} \simeq 1$, which may lead to a non-physical change in high-frequency resistivity.

Further, Eq. (3) and similar equations in [27,28] represent the expansion of cell impedance into an infinite series of alternating RC- and RL-circuits throughout the whole frequency range. For PEMFC spectra, this expansion is meaningful in the low-frequency domain. However, in the medium- and high-frequency range PEMFCs do not have inductive components and Eq. (3) could lead to less accurate results.

Another approach was suggested by Huang et al. [28], who proposed using the classic Debye kernel and letting γ be negative. In this way, the inductive component of the impedance is modeled as the sum of the impedances of parallel RC-circuits with a negative resistivity R. However, numerical examples in [28] show that the accuracy of inductive loop fitting is not high, seemingly because the Debye kernel with negative R is not a suitable basis for expanding

inductive impedance. Similar idea was suggested by Schiefer et al. [29], who proposed modifying the classic DRT by including *RC*-elements with negative resistance *R* in the low-frequency domain. However, the experimental spectra fitted using the calculated DRT were not presented in their work.

Below, we compare the DRT and DTT with the physics-based modeling (PBM) results using three experimental spectra of real PEM fuel cells. The PBM fitted to the spectra provides the basis for the comparison. We show that in general, the DTT predicts the process resistivities more accurately than the DRT. In one spectrum, the DTT resolves a peak which is missing in the DRT. Further, we suggest a simple modification of the composite kernel which allows to describe the inductive loop keeping the DTT function non-negative. We demonstrate that the DTT with the modified kernel provides a good fitting of the experimental spectrum with a low-frequency inductive loop.

2. Physics-based impedance model

The basic model assumptions are as follows:

1. The cell is isothermal, and the gaseous components obey the ideal gas law.
2. The electron conductivity of the porous layers is high. Variation of the electron potential can be ignored.
3. The ORR rate obeys the Tafel law.
4. The air flow in the cathode channel is described by the plug-flow equation.
5. The transport of liquid water through the gas-diffusion layer and the cathode channel is ignored.
6. The total flux of liquid water in the membrane is proportional to the cell current density. In previous versions of the model [25, 30], this flux was assumed to be zero. Here, this assumption is relaxed.

Table 1 shows the system of transient model equations for the transport of oxygen in the channel, Eq. (5), GDL, Eq. (6), and CCL, Eq. (7). The table also shows the equations for the transport of protons, Eq. (8), liquid water, Eq. (9), and water vapor, Eq. (10), in the CCL. We assume that at the CCL/GDL interface, the water vapor concentration is equal to the saturation concentration $c_v^s(T)$. Under this assumption, the solution to Eq. (10) is $c_v = c_v^s$, the evaporation rate $Q_{lv} = 0$, and the water vapor concentration perturbation amplitude is zero: $c_v^1 = 0$.

The lower part of Table 1 shows the expressions for the source terms in Eqs. (7)–(10) and the assumed formula for the water retention curve, Eq. (13). It also shows the parametric dependencies of the CCL proton conductivity and oxygen diffusivity on liquid saturation, Eqs. (14) and (15), respectively.

The boundary conditions describe the continuity of oxygen concentration and flux at the channel/GDL and GDL/CCL interfaces. They also describe zero oxygen flux in the membrane and zero proton current at the CCL/GDL interface; see [25,30] for further details. The incoming liquid water flux from the membrane to the CCL was described as

$$-\frac{K_l}{V_l\mu_l}\frac{\partial p_l}{\partial x} = \frac{\alpha_w j_0}{F} \tag{16}$$

where α_w is the net water transfer coefficient through the membrane.

Eqs. (5)–(10) were linearized and Fourier-transformed to obtain a system of linear equations for small AC perturbation amplitudes in the ω-space. Details of this procedure can be found in [25].

The flow field with the meander-like channel used in experiments was modeled as a single, straight channel. In all experiments, the cell current density was fixed at 0.1 A cm^{-2}, while the air flow stoichiometry was varied. To account for the non-uniformity of the local oxygen concentration and current density along the cell surface, the cathode side was divided into eight virtual segments. Segment 1 was at the channel inlet and segment 8 was at the outlet. In each segment, the through-plane problem was solved iteratively, along with the linearized

Table 1
Eqs. (5)–(10), the governing equations for oxygen, water and proton transport. Eqs. (11), (12), the ORR and evaporation/condensation rates, respectively. Eqs. (13), (14), (15) — WRC, proton conductivity vs saturation, and oxygen diffusivity vs saturation, respectively. For the notations see Nomenclature section.

Transport equations		
$\frac{\partial c_h}{\partial t} + v\frac{\partial c_h}{\partial z} = -\frac{D_b}{h}\frac{\partial c_b}{\partial x}\Big\|_{x=l_l+l_b}$	(5)	Channel
$\frac{\partial c_b}{\partial t} - D_b\frac{\partial^2 c_b}{\partial x^2} = 0$	(6)	GDL
$\frac{\partial c}{\partial t} - \frac{\partial}{\partial x}\left(D_{ox}\frac{\partial c}{\partial x}\right) = -\frac{Q_{ORR}}{4F}$	(7)	CCL
$C_{dl}\frac{\partial \eta}{\partial t} - \frac{\partial}{\partial x}\left(\sigma_p\frac{\partial \eta}{\partial x}\right) = -Q_{ORR}$	(8)	
$\frac{1}{V_l}\frac{\partial s}{\partial t} - \frac{K_l}{V_l\mu_l}\frac{\partial^2 p_l}{\partial x^2} = \frac{Q_{ORR}}{2F} - \frac{Q_{lv}}{2F}$	(9)	
$\frac{\partial c_v}{\partial t} - D_v\frac{\partial^2 c_v}{\partial x^2} = \frac{Q_{lv}}{2F}$	(10)	
Source functions		
$Q_{ORR} = i_*\left(\frac{c}{c_{ref}}\right)\exp\left(\frac{\eta}{b}\right)$	(11)	ORR rate
$Q_{lv} = \frac{2e_0\kappa\xi_{lv}RT}{l_t}\left(c_v^s - c_v\right)$	(12)	Evap. rate
Water retention curve (WRC) and the CCL transport coefficients		
$s = s_0 + \frac{(1-s_0)}{2}\left(1+\tanh\left(\frac{p_c - p_{c,0}}{k_{pc}}\right)\right)$	(13)	WRC
$\sigma_p = k_\sigma s$	(14)	H^+ conductivity
$D_{ox} = D_{ox,d}(1-s)^2$	(15)	O_2 diffusivity

and Fourier-transformed version of Eq. (5). The segment impedance Z_{seg} was calculated as

$$Z_{seg} = -\frac{\eta^1}{\sigma_p\partial\eta^1/\partial x}\Big|_{x=0} \tag{17}$$

where η^1 is the perturbation amplitude of the ORR overpotential, σ_p is the CCL proton conductivity, the through-plane coordinate x is counted from the membrane, and the superscript 1 marks the small perturbation amplitude. The total cell impedance was calculated as

$$Z_{cell} = \left(\frac{1}{N}\sum_{n=1}^{N}\frac{1}{Z_{seg,n}}\right)^{-1} + \mathrm{i}\omega L_{cab}S_{cell} + R_\infty, \tag{18}$$

where $N = 8$ is the number of segments, $L_{cab} = 20$ nH is the cable inductance, S_{cell} is the cell active area, and R_∞ is the high-frequency (ohmic) cell resistance. The value of L_{cab} has been determined through preliminary spectra fitting with L_{cab} as a parameter.

The experimental spectra were fitted using a Python constrained optimization module *least_squares* from the SciPy library. The nonlinear boundary-value problems (BVPs) for the static, through-plane shapes of the oxygen concentration c^0 and overpotential η^0, as well as the linear BVPs for the perturbation amplitudes c^1 and η^1 were solved using the SciPy *solve_bvp* module. Here, the superscript 0 marks the static values. The complex-valued linear BVPs were converted to real-valued equations for the real and imaginary parts of the unknown functions.

3. DRT and DTT techniques

The DTT spectrum follows Eq. (1) with a composite kernel K_c instead of K_D:

$$Z_{cell}(\omega) = R_\infty + R_{pol}\int_{-\infty}^{\infty} K_c(\omega,\tau)\,\gamma(\tau)\,d\ln\tau \tag{19}$$

The kernel K_c was designed to more accurately describe transport processes within the cell [11]

$$K_c(\omega,\tau)=\frac{\tanh\left(\alpha\sqrt{i\omega\tau}\right)}{\alpha\sqrt{i\omega\tau}\,(1+i\omega\tau)^{1-\beta}\left(\sqrt{i\omega\tau}\tanh\sqrt{i\omega\tau}\right)^{\beta}}, \tag{20}$$

and α, β are the step functions:

$$\alpha(\tau,\tau_\alpha)=\begin{cases}0, & \tau\le\tau_\alpha\\ 1, & \tau>\tau_\alpha\end{cases},\quad \beta(\tau,\tau_\beta)=\begin{cases}1, & \tau\le\tau_\beta\\ 0, & \tau>\tau_\beta\end{cases} \tag{21}$$

with $\tau_\beta<\tau_\alpha$. In the low-frequency (large τ) region $\alpha=1$, $\beta=0$ and K_c reduces to the transport layer kernel [31]

$$K_{TL}=\frac{\tanh\sqrt{i\omega\tau}}{\sqrt{i\omega\tau}\,(1+i\omega\tau)} \tag{22}$$

In the middle-frequency domain, we set $\alpha=0$, $\beta=0$ and K_c reduces to the standard Debye kernel, Eq. (2). In the high-frequency (small τ) domain, $\alpha=0$, $\beta=1$ and K_c takes the form of the proton transport kernel K_p [31]

$$K_p=\frac{1}{\sqrt{i\omega\tau}\tanh\sqrt{i\omega\tau}} \tag{23}$$

To describe the inductive loop, the DTT kernel Eq. (20) was modified by adding an inductive kernel in the lowest frequency region. The modified composite kernel (or m-composite kernel) K_{mc} is

$$K_{mc}(\omega,\tau)=\left(\frac{\tanh\left((\alpha-\zeta)\sqrt{i\omega\tau}\right)}{(\alpha-\zeta)\sqrt{i\omega\tau}\,(1+i\omega\tau)^{1-\zeta}\left(1+(i\omega\tau)^{-1}\right)^{\zeta}}\right)\times\left(\frac{1+i\omega\tau}{\sqrt{i\omega\tau}\tanh\sqrt{i\omega\tau}}\right)^{\beta}, \tag{24}$$

where ζ is a third step function

$$\zeta(\tau,\tau_\zeta)=\begin{cases}0, & \tau\le\tau_\zeta\\ 1, & \tau>\tau_\zeta\end{cases},\quad \text{where } \tau_\zeta>\tau_\alpha. \tag{25}$$

In other words, ζ is unity in the lowest frequency domain and it is zero otherwise. In the large τ (lowest frequency) region $\tau\ge\tau_\zeta$, we set $\alpha=\zeta=1$, $\beta=0$ and Eq. (24) reduces to the inductive RL-kernel, while for $\tau<\tau_\zeta$, the kernel Eq. (24) coincides with K_c, Eq. (20):

$$K_{mc}(\omega,\tau)=\begin{cases}\dfrac{1}{1+(i\omega\tau)^{-1}}, & \tau\ge\tau_\zeta\\ K_c,\ \text{Eq. (20)}, & \tau<\tau_\zeta.\end{cases} \tag{26}$$

If the spectrum contains an inductive loop, the cell polarization resistance R_{pol} is not known in advance and the DTT $\gamma_L(\tau)$ is obtained from the equation

$$Z_{cell}=R_{LF}\int_{-\infty}^{\infty}K_{mc}(\omega,\tau)\,\gamma_L(\tau)\,d(\ln\tau) \tag{27}$$

where R_{LF} is the real part of the cell impedance measured at the lowest frequency, i.e., R_{LF} includes the HFR (see discussion below). The subscript L indicates that the DTT γ_L determined from Eq. (27) differs from the one resulting from Eq. (19). The numerical method for calculating DRT and DTT spectra is described in [11].

4. Experimental

Experimental work was conducted at the Hawaii Natural Energy Institute using a custom-built fuel cell test station and impedance spectroscopy system [32]. Two catalyst coated membranes (CCMs) with active areas of 76 cm^2 (A76) and 5 cm^2 (C5) were used in this study.

The C5 sample was fabricated in-house using a Nafion XL membrane (20–25 μm thickness). The anode and cathode electrodes were applied to the membrane via an airbrush spraying method. The anode employed a 50% Pt/Vulcan XC-72 catalyst (E-TEK), while the cathode used a 40% Pt/Vulcan XC-72 catalyst (E-TEK). An aqueous solution of Aquivion EW-830 (24 wt%) was used as the ionomer binder, with a final dry content of 33% [33–35]. The anode and cathode had platinum loadings of 0.43 and 0.45 mg_{Pt} cm^{-2}, respectively, with a resulting electrode thickness of 8–10 μm.

The C5 sample was assembled into a 5 cm^2 test hardware with 25BC gas diffusion layers (GDLs) on both the anode and cathode sides. A 200 μm thick Teflon gasket was used to achieve 20% compression. The 5 cm^2 hardware (Fuel Cell Technologies Inc.) featured a single-channel serpentine flow field design for both electrodes arranged in a co-flow configuration. Operating conditions for C5 were as follows: anode/cathode gases were H_2/air, with flow rates of 0.3/0.5 l min^{-1}, relative humidities of 100%/50%, pressure of 150 kPa, and temperature of 80 °C. Reagent flow rates were fixed.

A commercial CCM from Gore, with identical anode and cathode platinum loadings of 0.4 mgPt cm^{-2}, was used for the A76 sample. The electrode thickness was 11–12 μm. 25BC GDLs were employed on both the anode and cathode sides. Teflon gaskets with a thickness of 125 μm provided appropriate compression of 25%–30% for the large active area MEA. The A76 sample was assembled in custom-designed hardware with 10-channel serpentine flow fields in a co-flow configuration. The sample evaluation was conducted under the following conditions: anode/cathode gases were H_2/air, with relative humidities of 100%/50%, pressure of 150 kPa, and temperature of 80 °C. Reagent stoichiometries of 2/2 and 2/4 were used. A summary of the operating conditions is presented in Table 2.

EIS measurements for both samples were performed under galvanostatic control at a bias current density of 100 mA cm^{-2}. The perturbation current was adjusted to ensure that the resulting cell voltage fluctuation remained below 10 mV. The frequency range for the impedance sweep was from 10 kHz to 0.1 Hz. The impedance spectra were recorded with 15 steps/ decade for the C5 sample and 11 steps per decade for the A76 sample.

Typically, the frequency range from 10 kHz to 0.1 Hz adequately captures the main electrochemical and transport processes in the cell. At high frequencies, clear impedance response is limited by cable inductance, while at low frequencies the main obstacle is the long acquisition time required to achieve an acceptable signal-to-noise ratio. For example, recording a spectrum from 10 kHz to 0.1 Hz with 11 points per decade takes 15–20 min, whereas extending the lower limit to 0.05 Hz increases the measurement time to 40–50 min or more.

Since EIS requires that the system remain in steady state without significant potential or current drift during the acquisition, measurements extending over such long time periods may suffer from instability, which reduces the quality of the results. This practical consideration guided our choice of the 0.1 Hz lower frequency limit.

5. Results and discussion

5.1. Spectra without an inductive loop

The DRT and DTT spectra consist of a number of peaks, with the area under the peak giving the contribution of the respective process to the total cell polarization resistance. Comparing the PBM resistivities with the DRT and DTT peak resistivities is only possible in the small-current regime of the cell operation [36]:

$$j_0\ll\min\left\{j_p=\frac{\sigma_p b}{l_t},\ j_{ox}=\frac{4FD_{ox}c_1}{l_t}\right\} \tag{28}$$

Here, j_0 is the cell current density, j_p, j_{ox} are the characteristic current densities for the proton and oxygen transport in the CCL, respectively, σ_p is the CCL proton conductivity, b the ORR Tafel slope, l_t the CCL thickness, D_{ox} the CCL oxygen diffusivity, and c_1 the oxygen concentration at the CCL/GDL interface. Eq. (28) guarantees that the overpotential distribution through the CCL depth is nearly constant.

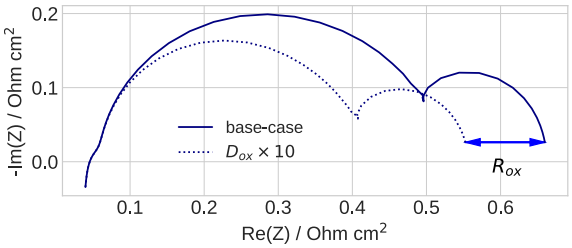

Fig. 1. The schematic illustrating the calculation of the oxygen transport resistivity using the PBM. First, the PBM is fitted to the experimental spectrum. The resulting model spectrum is shown by the solid line. Next, the CCL oxygen diffusivity is multiplied by ten, and a new model spectrum is calculated, shown by the dotted line. The difference in polarization resistivities between the two spectra is the oxygen transport resistivity, R_{ox}.

Formally, the inductive loop in the impedance spectrum can be neglected if [22]

$$\frac{\partial \sigma_p}{\partial j_0} \ll \beta \sigma_p^{OCV} \tag{29}$$

Here, σ_p^{OCV} is the CCL proton conductivity at open-circuit conditions and $\beta \lesssim 1$ cm^2 A^{-1} is an empirical parameter describing the rate of the proton conductivity growth with the cell current density due to water produced in the ORR [22]. Eq. (29) indicates that the variation of the CCL proton conductivity with the cell current density must be small.

If Eq. (28) holds, the total polarization resistivity of the cell is a sum of the partial resistivities [37,38]:

$$R_{pol} = R_{chan} + R_{GDL} + R_{ORR} + R_{CCL} + R_p \tag{30}$$

where R_{chan} is the resistivity associated with the oxygen transport in the channel, R_{GDL} is the resistivity due to oxygen transport in the GDL, R_{ORR} is the faradaic resistivity, R_{CCL} is the resistivity due to oxygen transport in the CCL, and R_p is the CCL proton transport resistivity.

However, if Eq. (28) is violated, breaking up R_{pol} into its components, Eq. (30), is impossible. In that case, the transport and faradaic processes in the CCL are coupled nonlinearly, creating interdependencies between them. This means that, although the DRT and DTT still produce a set of peaks, the resistivity of each peak may depend on multiple processes within the cell [39].

In the following, the resistivities due to oxygen transport in the channel, GDL and CCL will be referred to as "channel", "GDL" and "CCL" resistivities, respectively. The resistivity due to proton transport in the CCL is referred to as "proton" resistivity.

The physics-based cell parameters were determined as follows: First, the PBM (Section 2) has been fitted to the experimental spectrum. The resulting fitting parameters include the ORR Tafel slope b, the CCL proton conductivity σ_p and oxygen diffusivity D_{ox}, and the GDL oxygen diffusivity D_b. To determine the CCL resistivity, the parameter D_{ox} was multiplied by a factor of ten, and a new model spectrum with the updated D_{ox} was calculated. The CCL resistivity was then calculated as the difference in polarization resistance between the new and old spectra (Fig. 1). The similar procedure was used to determine the channel, GDL, and the proton resistivity, by varying λ, D_b and σ_p, respectively.

Fig. 2 shows the experimental and fitted model spectra of large cell A76, which has a surface area of 76 cm^2 (see the Experimental section for the further details). The cell operating parameters listed in Table 2 are typical for real applications. In particular, the low air flow stoichiometry ($\lambda = 2$) results in a distinct low-frequency arc in the Nyquist spectrum (Fig. 2a) [40].

The DRT and DTT spectra were calculated using the real part of impedance (Fig. 3). The DRT spectrum contains three peaks (Fig. 3a). The leftmost, low-frequency peak is undoubtedly due to oxygen

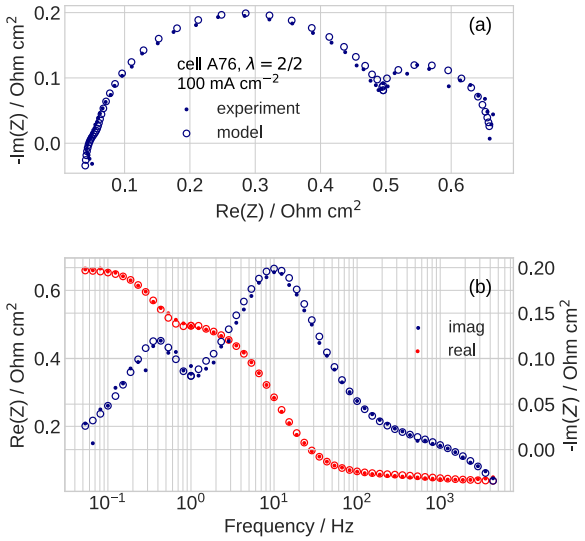

Fig. 2. (a) The experimental (dots) and fitted PBM (open circles) spectra of the cell A76 at the air flow stoichiometry of 2 and current density of 100 mA cm^{-2}. (b) The Bode plots of the real and imaginary parts of the impedances in (a).

Table 2
The operating and geometrical parameters of the tested cells.

Cell ID	A76	C5
Cell active area, cm^2	76	5
Anode/cathode feed	H_2/air	
Current density, mA cm^{-2}	100	
Cathode relative humidity RH,	0.5	
Cathode pressure, bar	1.5	
Cell temperature, K	273+80	
Cathode flow stoichiometry	2/2, 2/4	$\gg 10$
CCL thickness, μm	12	8.2
GDL thickness, μm	235	

transport in the channel (the "chan" peak in Fig. 3a). The rightmost, high-frequency peak can be attributed to the proton transport in the CCL (the "proton" peak, Fig. 3a). In the absence of separate peaks for the ORR and oxygen transport in the GDL and CCL, we must assume that the remaining large peak comprises the faradaic and oxygen transport in the porous layers (the "GDL+ORR+CCL" peak in Fig. 3a).

Fig. 3b shows the advantage of DTT over DRT. The DTT spectrum resolves the peak due to oxygen transport in the GDL (the "GDL" peak in Fig. 3b). The neighboring medium-frequency peak accumulates the faradaic resistivity and the resistivity due to oxygen transport in the CCL (the "ORR+CCL" peak in Fig. 3b). Note that the position of the step of the α-function in Fig. 3b is chosen right below the "ORR+CCL" peak and the step of the β-function is taken to be in the middle of the "proton" peak. The latter choice provides the position of the proton peak close to the position of that peak in the DRT spectrum.

Fig. 4 compares the peak resistivities calculated from the DRT and DTT spectra with those derived from the PBM. As can be seen, the GDL resistivity obtained from the DTT is in good agreement with the PBM value. The DRT provides a quite accurate channel resistivity and the sum of the GDL, ORR, and CCL resistivities (the large peak in Fig. 3a), whereas the DTT proton resistivity is more precise than the DRT one (Fig. 4).

Fig. 5 shows the DRT and DTT spectra of the same cell under twice the stoichiometry λ of the air flow. In this regime, the GDL peak merges with the ORR peak in both the DRT and DTT spectra; however, the CCL peak is well resolved (Fig. 5a,b). Higher stoichiometry shifts the "channel" peak to higher frequencies (cf. Figs. 3 and 5). In addition, the higher λ presumably changes the distribution of water in the porous

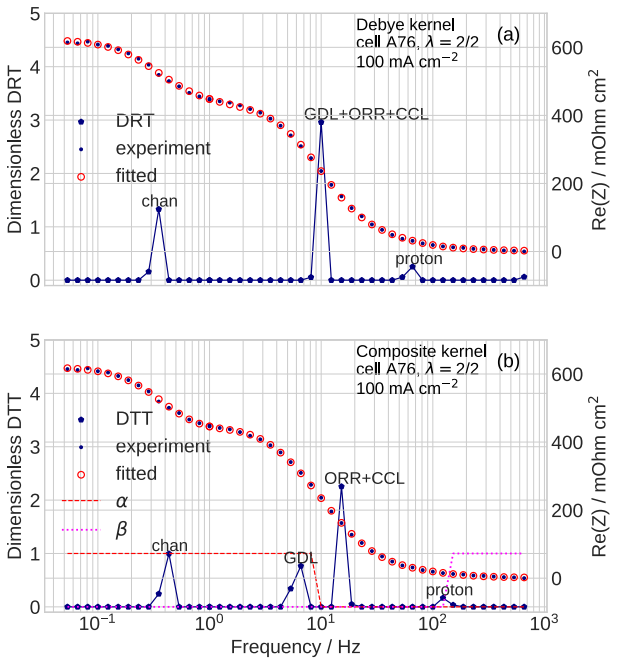

Fig. 3. (a) DRT and (b) DTT spectra of the cell A76 at the current density of 100 mA cm^{-2} and the air flow stoichiometry of 2. The dashed lines indicate the α and β step functions. For the cell parameters and the regime of cell operation see Table 2.

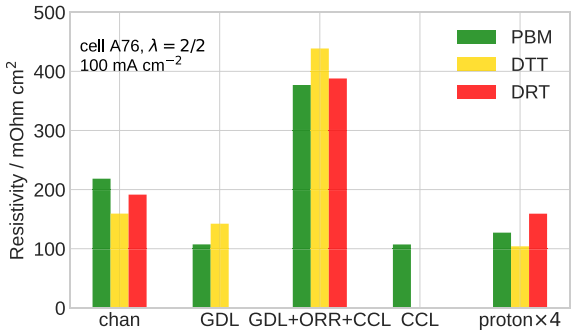

Fig. 4. Comparison of the partial resistivities of the cell A76 resulting from the PBM, DTT, and DTT.

layers, shifting the frequency position of the GDL and CCL peaks. This shift merges the GDL peak with the ORR one and makes the CCL peak visible. At $\lambda = 4$, both the DRT and DTT return the resistivities that are close to each other (Fig. 6). Note that the PBM makes it possible the reliable attribution of the DRT and DTT peaks.

5.2. Spectrum with the inductive loop

The last example is the spectrum of the small cell C5 with an active surface area of 5 cm^2 (Table 2). The Nyquist spectrum of this cell contains a distinct inductive loop (Fig. 7a). Attempting to fit this spectrum using the standard DRT with the Debye kernel fails.

Fig. 8 shows the DTT spectrum of the cell C5 calculated using the m-composite kernel K_{mc}, Eq. (24), and both the real and imaginary parts of the experimental impedance. As can be seen, the solution of Eq. (27) fits well the Nyquist spectrum (Fig. 8a). Fig. 8b shows that two processes marked as "loop1" and "loop2" contribute to the inductive loop. The quality of the Nyquist spectrum fitting with the standard DRT is extremely poor and it is not shown here.

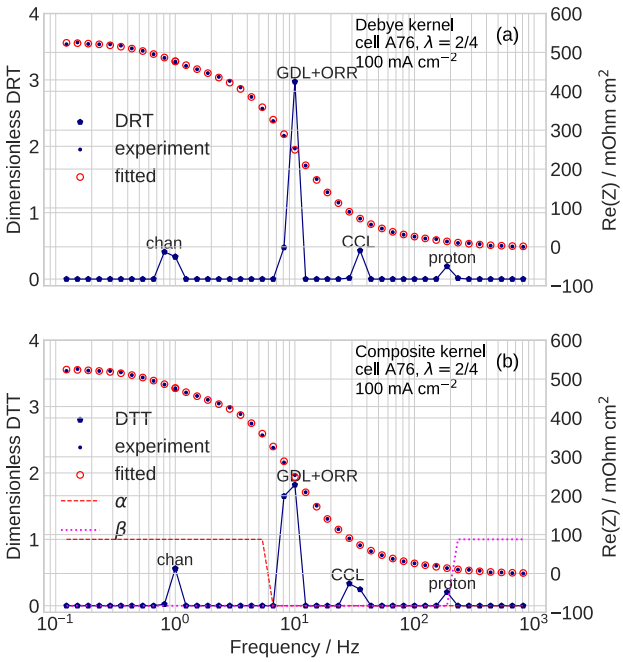

Fig. 5. The same as in Fig. 3 for the regime with the air flow stoichiometry of 4.

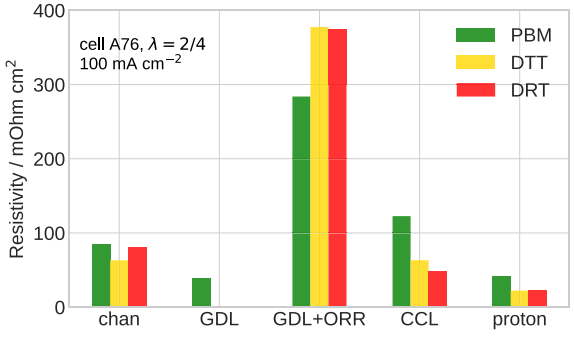

Fig. 6. The same as in Fig. 4 for the regime with the air flow stoichiometry of 4.

Table 3
The resistivities of the DTT peaks in Fig. 8b. The last row shows the ratio $R_{LF}/(R_\infty + R_{pol}) \equiv 1 + \epsilon$ calculated from the DTT. Note that the sum of the peak resistivities includes the HFR, see Eq. (27).

Peak ID	Peak resistivity mOhm cm^2
loop1	22.4
loop2	26.8
GDL+ORR	659
CCL	21.7
proton	8.50
Ratio $\dfrac{R_{LF}}{R_\infty + R_{pol}}$	1.0538

We do not compare the resistivities of the peaks in Fig. 8b to the parameters resulting from the PBM fitting because the PBM may not give the true static resistivity of the cell. In its present form, the PBM takes into account a single process that leads to the inductive loop. This process is the slow relaxation of the CCL proton conductivity upon variation of the CCL liquid water content with the cell current density.

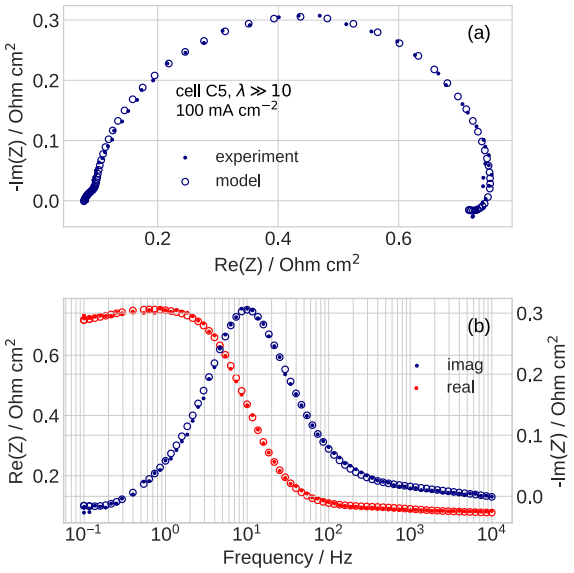

Fig. 7. (a) The experimental Nyquist spectrum (solid points) and fitted physics-based model (open circles) of the cell C5. For the cell parameters and operation regime see Table 2. (b) The Bode plots of the real and imaginary parts of the impedances in (a).

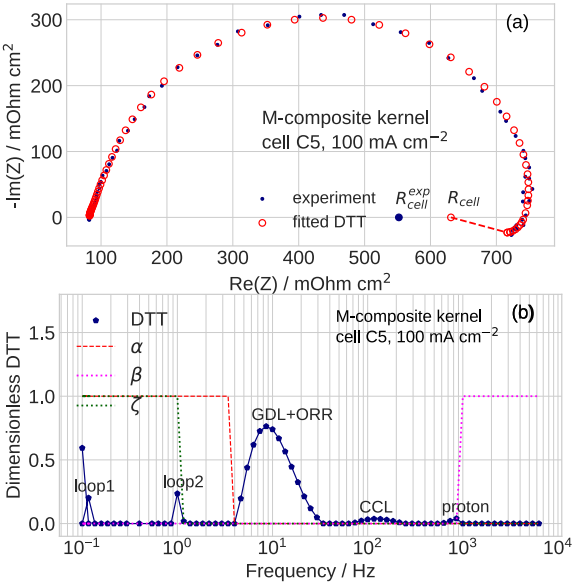

Fig. 8. (a) The experimental Nyquist spectrum (blue solid points) of the cell C5 and the spectrum fitted using the DTT with the modified kernel Eq. (24) (red open circles). The cell current density is 100 mA cm^{-2} and the air flow stoichiometry is large. $R_{cell} = R_{pol} + R_{HFR}$ indicates the sum of the cell static polarization resistivity and HFR calculated from the DTT, R_{cell}^{exp} shows the cell static resistivity calculated from the polarization curve. (b) The DTT spectrum calculated using the m-composite kennel, Eq. (24). The dashed lines indicate the α, β and ζ step functions. For the cell parameters and the regime of cell operation see Table 2.

In contrast, the DTT in Fig. 8b shows two processes contributing to the inductive loop.

The peak resistivities returned by the DTT (Table 3) allow us to estimate the cell static differential resistivity R_{cell}, which is a sum of the HFR and the cell polarization resistivity R_{pol}:

$$R_{cell} = R_\infty + R_{pol} \tag{31}$$

Since R_{pol} is not known in advance, Eq. (27) is solved using R_{LF} as the normalization constant. The numerical solution gives

$$\int_{-\infty}^{\infty} \gamma_L(\tau)\, d\ln\tau = 1 + \epsilon \tag{32}$$

where $\epsilon > 0$ is a positive constant. On the other hand, if R_{pol} were known, and $R_{LF} = R_\infty + R_{pol}$ were taken, the integral in Eq. (32) would equal to 1. Indeed, it is easy to show that as $\omega \to 0$, the m-composite kernel Eq. (24) tends to unity for all τ, except the large τ domain, where it tends to zero. Thus, with $R_{LF} = R_\infty + R_{pol}$ in Eq. (27), the DTT γ_L would satisfy the normalization condition

$$\int_{-\infty}^{\infty} \gamma_L(\tau)\, d\ln\tau = 1 \tag{33}$$

which is obtained by setting $\omega \to 0$ in Eq. (34)

$$Z_{cell}(\omega) = \left(R_\infty + R_{pol}\right) \int_{-\infty}^{\infty} K_{mc}(\omega,\tau)\, \gamma_L(\tau)\, d\ln\tau. \tag{34}$$

Only the three rightmost peaks in Fig. 8a contribute to the cell DC resistivity. Thus, to calculate $R_{cell} = R_\infty + R_{pol}$ we have to sum the resistivities from the rows "GDL+ORR", "CCL" and "proton" in Table 3 and divide the result by the normalization factor $1+\epsilon$, which is 1.0538 in this case (the last row in Table 3):

$$R_{cell} = \frac{1}{\epsilon}\left(R_3 + R_4 + R_5\right) \tag{35}$$

where the peaks in Fig. 8b are numbered from left to right. Evidently, the polarization resistivity R_{pol} is

$$R_{pol} = R_{cell} - R_\infty \tag{36}$$

where R_∞ is the leftmost point of the spectrum (HFR) in Fig. 8a.

The resulting $R_{cell} = 654$ mOhm cm^2 is shown in Fig. 8a as an open red circle. For comparison, the experimental polarization curve of the cell was interpolated using the cubic spline. Differentiation of the spline leads to $R_{cell}^{exp} = 552$ mOhm cm^2, which is shown in Fig. 8a as a large blue solid point. The hundred mOhm cm^2 discrepancy between the DTT-predicted and experimental values of the cell resistivity is due to the lack of measured points in the frequency range below 0.1 Hz.

Suppose that the low-frequency points are measured and an accurate value of R_{pol} can be found using the procedure above. The contribution of non-inductive peaks into the true polarization resistivity can be calculated as follows. For the sum of the non-inductive peak resistivities we can write

$$R_3 + R_4 + R_5 = \epsilon\left(R_\infty + R_{pol}\right) = \epsilon\left(\frac{R_\infty}{R_{pol}} + 1\right) R_{pol} \tag{37}$$

From Eq. (37) we get

$$\frac{R_3}{k_\epsilon} + \frac{R_4}{k_\epsilon} + \frac{R_5}{k_\epsilon} = R_{pol}, \quad \text{where} \quad k_\epsilon = \epsilon\left(\frac{R_\infty}{R_{pol}} + 1\right). \tag{38}$$

Thus, for the true contribution R_i^* (Ohm cm^2) of the ith non-inductive process into the cell polarization resistivity R_{pol} we find a simple formula

$$R_i^* = \frac{R_i}{\epsilon\left(1 + R_\infty/R_{pol}\right)} \tag{39}$$

In some works, the DRT of a spectrum containing an inductive loop is calculated discarding the LF points with the positive imaginary part. Fig. 8a shows that this procedure may lead to misleading results, since the rightmost point where the Nyquist spectrum crosses the real axis may strongly differ from the true DC resistivity R_{cell}^{exp} of the cell.

Fig. 9 shows a screenshot of the running code calculating the DTT for the spectrum with an inductive loop. Using the mouse pointer, the α-, β-, and ζ-steps can be moved along the frequency axis by moving the sliders (Fig. 9b). The fitted real and imaginary parts of impedance in Fig. 9a are recalculated in real time according to the current steps positioning.

It is worth noting that the simplest RL-kernel, Eq. (26), may not be suitable for expanding an inductive loop. For example, the loop due

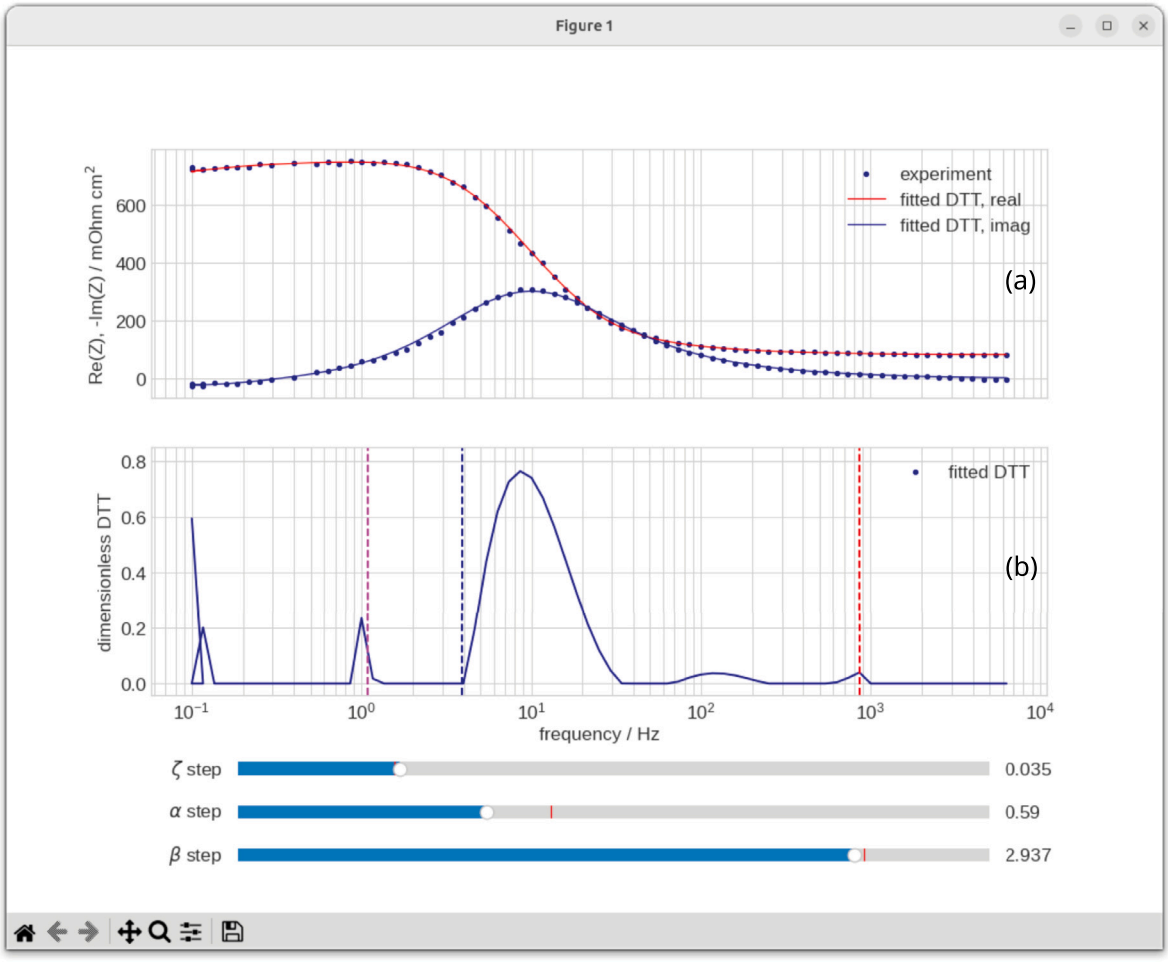

Fig. 9. A screenshot of the running code for calculations of DTT with the m-composite kernel from the spectrum in Fig. 8a. (a) The Bode plots of the experimental real and imaginary parts of impedance (solid points) and the fitted DTT γ_L (lines). (b) The DTT (solid line) and the ζ-, α-, and β-steps (dotted vertical lines: magenta for the ζ-step, blue for the α-step, and red for the β-step). The sliders below allow to adjust the position of the steps along the frequency axis using the mouse pointer. The fitted DTT spectra in (a) are recalculated in real time according to the steps positioning.

to the slow relaxation of the CCL proton conductivity is not described by the RL-impedance [22]. Physics-based modeling of low-frequency processes in PEM fuel cells is a subject of ongoing research and a better basis for an experimental "inductive" loop could be established when this work is completed.

Note also that a DTT spectrum is particularly sensitive to the frequency position $f_\beta = 1/(2\pi\tau_\beta)$ of the step of the β-function, Eq. (21). In all of the above examples, f_β was chosen to maximize the height of the ORR and CCL peaks while shifting the proton peak as little as possible compared to its position in the DRT spectrum.

The DTT with the modified composite kernel (Eq. (24)) can be used to analyze impedance spectra from PEM fuel cells. However, the applicability of this technique to other types of fuel cells, such as DMFC and SOFC, has not been verified. The proposed DTT is not suitable for analyzing the impedance spectra of lithium-ion batteries.

5.3. Selecting the frequencies for α-, β- and ζ-steps

The positioning of the α-, β- and ζ-steps on the frequency scale determines the domains, in which the sub-kernels (2), (22), (23) and the inductive (26) are in effect. The following recommendations for selecting the step positions are based on estimates of the characteristic frequencies in a typical PEM fuel cell [11].

- The characteristic frequency of the "channel" impedance typically does not exceed 1 Hz. The characteristic frequency of the GDL impedance is typically below 10 Hz. Thus, we recommend to place the step of the α-function at the frequency $\gtrsim 10$ Hz.
- The characteristic frequency of the proton transport in the CCL typically exceeds 1 kHz. Thus, the β-step can be set at the frequency around 1 kHz.
- The characteristic frequency of inductive processes in the cell is about 0.1 Hz. If the inductive loop is present, the ζ-step should be located at the frequency $\gtrsim 0.1$ Hz.

A good starting point for the positioning of the α and β steps provides the standard DRT spectrum. When the code is run, the calculated DRT is displayed on top of the DTT spectrum. However, when the inductive loop is present, calculation of DRT is meaningless and positioning of the α, β and ζ-steps is a matter of the user's intuition and experience. In all cases, the quality of the fit of the experimental spectra by the DTT, as displayed by the code, is a good indicator of this positioning.

6. Conclusions

The classic distribution of relaxation times (DRT) technique attempts to represent each transport and kinetic process in a PEM fuel cell as a sum of parallel RC-circuit impedances. However, the RC-circuit kernel is not an accurate basis for expanding the proton and oxygen transport processes. A better option is the composite basis function

(kernel), which "switches on" one of the three relevant kernels in the low-, medium, and high-frequency domains. In this study, we reported tests of the distribution of transport times (DTT) technique based on this kernel. We compared the cell parameters resulting from the DRT and DTT with those resulting from the fitting of the physics-based model to experimental cell impedance. Furthermore, incorporation of the inductive *RL*-kernel into the composite DTT kernel allows us to describe the spectrum with a low-frequency inductive loop.

The results can be summarized as follows:

- In general, the DTT yields more accurate process resistivities than the DRT.
- The DTT detects oxygen transport peaks that are missing in the DRT.
- The DTT with the modified composite kernel Eq. (24) describes well the spectrum with an inductive loop.
- In the absence of inductive loop, it can be recommended using the DTT together with the DRT for impedance spectra analysis.
- The spectrum with an inductive loop can be processed using the DTT with the m-composite kernel. To accurately describe the low-frequency loop, it is important to measure the spectra down to frequencies of 10 mHz or less.

CRediT authorship contribution statement

Tatyana Reshetenko: Writing – original draft, Supervision, Resources, Investigation, Data curation. **Andrei Kulikovsky:** Writing – review & editing, Writing – original draft, Visualization, Validation, Supervision, Software, Project administration, Methodology, Investigation, Formal analysis, Conceptualization.

Declaration of Generative AI and AI-assisted technologies in the writing process

The AI assistant DeepL was used solely to correct possible language errors. The authors are fully responsible for the content of the paper.

Declaration of competing interest

The authors declare that they have no known competing financial interests or personal relationships that could have appeared to influence the work reported in this paper.

Acknowledgments

T. Reshetenko gratefully acknowledges the funding from the US Office of Naval Research (N00014-22-1-2045). The authors are thankful to G. Randolf and J. Huizingh for their valuable assistance with operating the system.

Software for the DRT and DTT calculations

The link to the most recent version of the MS Windows exe-file for the DRT and DTT calculations is available at https://github.com/akulikovsky/DTT_software.

References

[1] Ö.F. Günaydin, S. Topçu, A. Aksoy, Hydrogen fuel cell vehicles: Overview and current status of hydrogen mobility, Int. J. Hydrog. Energy 142 (2025) 918–936, http://dx.doi.org/10.1016/j.ijhydene.2025.01.412.

[2] A. Lasia, Electrochemical Impedance Spectroscopy and Its Applications, Springer, New York, 2014.

[3] R. Fuoss, J. Kirkwood, Electrical properties of solids. VIII. Dipole moments in polyvinyl chloride-diphenyl systems, J. Am. Chem. Soc. 63 (1941) 385–394, http://dx.doi.org/10.1021/ja01847a013.

[4] H. Schichlein, A.C. Müller, M. Voigts, A. Krügel, E. Ivers-Tiffée, Deconvolution of electrochemical impedance spectra for the identification of electrode reaction mechanisms in solid oxide fuel cells, J. Appl. Electrochem. 32 (2002) 875–882, http://dx.doi.org/10.1023/A:1020599525160.

[5] S. Hershkovitz, S. Tomer, S. Baltianski, Y. Tsur, ISGP: Impedance spectroscopy analysis using evolutionary programming procedure, ECS Trans. 33 (2011) 67–73, http://dx.doi.org/10.1149/1.3589186.

[6] B.A. Boukamp, Fourier transform distribution function of relaxation times; application and limitations, Electrochim. Acta 154 (2015) 35–46, http://dx.doi.org/10.1016/j.electacta.2014.12.059.

[7] E. Ivers-Tiffée, A. Weber, Evaluation of electrochemical impedance spectra by the distribution of relaxation times, J. Ceram. Soc. Jpn. 125 (2017) 193–201, http://dx.doi.org/10.2109/jcersj2.16267.

[8] F. Ciucci, Modeling electrochemical impedance spectroscopy, Curr. Opin. Electrochem. 13 (2018) 132–139, http://dx.doi.org/10.1016/j.coelec.2018.12.003.

[9] N. Bevilacqua, M. Schmid, R. Zeis, Understanding the role of the anode on the polarization losses in high-temperature polymer electrolyte membrane fuel cells using the distribution of relaxation times analysis, J. Power Sources 471 (2020) 228469, http://dx.doi.org/10.1016/j.jpowsour.2020.228469.

[10] G.A. Cohen, D. Gelman, Y. Tsur, Development of a typical distribution function of relaxation times model for polymer electrolyte membrane fuel cells and quantifying the resistance to proton conduction within the catalyst layer, J. Phys. Chem. C 125 (2021) 11867–11874, http://dx.doi.org/10.1021/acs.jpcc.1c03667.

[11] A. Kulikovsky, Understanding impedance spectra of a PEM fuel cell via the distribution of transport times, Electrochim. Acta 539 (2025) 147063, http://dx.doi.org/10.1016/j.electacta.2025.147063.

[12] N. Wagner, E. Gülzow, Change of electrochemical impedance spectra (EIS) with time during CO–poisoning of the pt-anode in a membrane fuel cell, J. Power Sources 127 (2004) 341–347, http://dx.doi.org/10.1016/j.jpowsour.2003.09.031.

[13] O. Antoine, Y. Bultel, R. Durand, Oxygen reduction reaction kinetics and mechanism on platinum nanoparticles inside nafion, J. Electroanal. Chem. 499 (2001) 85–94, http://dx.doi.org/10.1016/S0022-0728(00)00492-7.

[14] R. Makharia, M.F. Mathias, D.R. Baker, Measurement of catalyst layer electrolyte resistance in PEFCs using electrochemical impedance spectroscopy, J. Electrochem. Soc. 152 (2005) A970–A977, http://dx.doi.org/10.1149/1.1888367.

[15] S.K. Roy, M.E. Orazem, Deterministic impedance models for interpretation of low frequency inductive loops in PEM fuel cells, ECS Trans. 3 (2006) 1031–1040, http://dx.doi.org/10.1149/1.2356222.

[16] S.K. Roy, M.E. Orazem, B. Tribollet, Interpretation of low-frequency inductive loops in PEM fuel cells, J. Electrochem. Soc. 154 (2007) B1378–B1388, http://dx.doi.org/10.1149/1.2789377.

[17] B.P. Setzler, T.F. Fuller, A physics–based impedance model of proton exchange membrane fuel cells exhibiting low–frequency inductive loops, J. Electrochem. Soc. 162 (2015) F519–F530, http://dx.doi.org/10.1149/2.0361506jes.

[18] I.A. Schneider, M.H. Bayer, A. Wokaun, G.G. Scherer, Impedance response of the proton exchange membrane in polymer electrolyte fuel cells, J. Electrochem. Soc. 155 (2008) B783–B792, http://dx.doi.org/10.1149/1.2929823.

[19] K. Wiezell, P. Gode, G. Lindbergh, Steady-state and EIS investigations of hydrogen electrodes and membranes in polymer electrolyte fuel cells: I. Mmodeling, J. Electrochem. Soc. 153 (2006) A749, http://dx.doi.org/10.1149/1.2172559.

[20] H. Holmström, K. Wiezell, G. Lindbergh, Studying low-humidity effects in PEFCs using EIS: I. Experimental, J. Electrochem. Soc. 159 (2012) F369, http://dx.doi.org/10.1149/2.005208jes.

[21] Q. Meyer, C. Zhao, Air perturbation-induced low-frequency inductive electrochemical impedance arc in proton exchange membrane fuel cells, J. Power Sources 488 (2021) 229245, http://dx.doi.org/10.1016/j.jpowsour.2020.229245.

[22] A. Kulikovsky, Effect of proton conductivity transients on PEM fuel cell impedance: Formation of a low–frequency inductive loop, Electrochem. Comm. 140 (2022) 107340, http://dx.doi.org/10.1016/j.elecom.2022.107340.

[23] I. Pivac, F. Barbir, Inductive phenomena at low frequencies in impedance spectra of proton exchange membrane fuel cells – A review, J. Power Sources 326 (2016) 112–119, http://dx.doi.org/10.1016/j.jpowsour.2016.06.119.

[24] C. Gerling, M. Hanauer, U. Berner, K.A. Friedrich, Experimental and numerical investigation of the low-frequency inductive features in differential pemfcs: Ionomer humidification and platinum oxide effects, J. Electrochem. Soc. 170 (2023) 014504, http://dx.doi.org/10.1149/1945-7111/acb3ff.

[25] Y. Sun, T. Kadyk, A. Kulikovsky, M. Eikerling, The effect of liquid saturation transients on PEM fuel cell impedance: Inductive loop and instability of catalyst layer operation, J. Electrochem. Soc. 171 (2024) 074506, http://dx.doi.org/10.1149/1945-7111/ad5efd.

[26] M. Danzer, Generalized distribution of relaxation times analysis for the characterization of impedance spectra, Batteries 5 (2019) 1–16, http://dx.doi.org/10.3390/batteries5030053.

[27] C. Plank, T.G. Bergmann, N. Schlüter, M.A. Danzer, Distribution of relaxation times analysis for impedance spectra containing resistive–inductive characteristics: Part I. Deconvolution methods, J. Electrochem. Soc. 172 (2025) 060514, http://dx.doi.org/10.1149/1945-7111/adda7b.

[28] J. Huang, M. Papac, R. O'Hayre, Towards robust autonomous impedance spectroscopy analysis: A calibrated hierarchical Bayesian approach for electrochemical impedance spectroscopy (EIS) inversion, Electrochim. Acta 367 (2021) 137493, http://dx.doi.org/10.1016/j.electacta.2020.137493.

[29] A. Schiefer, M. Heinzmann, A. Weber, Inductive low-frequency processes in PEMFC-impedance spectra, Fuel Cells 20 (2020) 499–506, http://dx.doi.org/10.1002/fuce.201900212.

[30] T. Reshetenko, Y. Sun, T. Kadyk, M. Eikerling, A. Kulikovsky, An impedance spectroscopy study to unravel the effect of water on proton and oxygen transport in PEM fuel cells, Electrochim. Acta 507 (2024) 145172, http://dx.doi.org/10.1016/j.electacta.2024.145172.

[31] A. Kulikovsky, A kernel for PEM fuel cell distribution of relaxation times, Front. Energy Res. 9 (2021) 780473, http://dx.doi.org/10.3389/fenrg.2021.780473.

[32] T.V. Reshetenko, G. Bender, K. Bethune, R. Rocheleau, Systematic study of back pressure and anode stoichiometry effects on spatial PEMFC performance distribution, Electrochim. Acta 56 (2011) 8700–8710, http://dx.doi.org/10.1016/j.electacta.2011.07.058.

[33] Y. Garsany, R.W. Atkinson, B.D. Gould, K.E. Swider-Lyons, High power, low-Pt membrane electrode assemblies for proton exchange membrane fuel cells, J. Power Sources 408 (2018) 38–45, http://dx.doi.org/10.1016/j.jpowsour.2018.10.073.

[34] Y. Garsany, R.W. Atkinson, M.B. Sassin, R.M.E. Hjelm, B.D. Gould, K.E. Swider-Lyons, Improving PEMFC performance using short-side-chain low-equivalent-weight PFSA ionomer in the cathode catalyst layer, J. Electrochem. Soc. 165 (2018) F381, http://dx.doi.org/10.1149/2.1361805jes.

[35] M.B. Sassin, Y. Garsany, B.D. Gould, K.E. Swider-Lyons, Fabrication method for laboratory-scale high-performance membrane electrode assemblies for fuel cells, Anal. Chem. 89 (2017) 511–518, http://dx.doi.org/10.1021/acs.analchem.6b03005.

[36] A.A. Kulikovsky, The regimes of catalyst layer operation in a fuel cell, Electrochim. Acta 55 (2010) 6391–6401, http://dx.doi.org/10.1016/j.electacta.2010.06.053.

[37] A. Kulikovsky, O. Shamardina, A model for PEM fuel cell impedance: Oxygen flow in the channel triggers spatial and frequency oscillations of the local impedance, J. Electrochem. Soc. 162 (2015) F1068–F1077, http://dx.doi.org/10.1149/2.0911509jes.

[38] T. Reshetenko, A. Kulikovsky, PEM fuel cell characterization by means of the physical model for impedance spectra, J. Electrochem. Soc. 162 (2015) F627–F633, http://dx.doi.org/10.1149/2.1141506jes.

[39] A. Kulikovsky, A model–based analysis of PEM fuel cell distribution of relaxation times, Electrochim. Acta 429 (2022) 141046, http://dx.doi.org/10.1016/j.electacta.2022.141046.

[40] I.A. Schneider, S.A. Freunberger, D. Kramer, A. Wokaun, G.G. Scherer, Oscillations in gas channels. Part I. The forgotten player in impedance spectroscopy in PEFCs, J. Electrochem. Soc. 154 (2007) B383–B388, http://dx.doi.org/10.1149/1.2435706.